Superior transverse piezoelectricity in organic-inorganic hybrid perovskite nanorods for mechanical energy harvesting

Asif Abdullah Khan [a,*,1], Guangguang Huang [a,b,1], Md Masud Rana [a], Nanqin Mei [c], Margherita Biondi [d], Shazzad Rassel [a], Nicolas Tanguy [e], Bin Sun [d], Zoya Leonenko [c], Ning Yan [e], Chunlei Wang [f], Shuhong Xu [f], Dayan Ban [a,g,h]

[a] Waterloo Institute for Nanotechnology, University of Waterloo, 200 University Ave West, Waterloo N2L 3G1, ON, Canada
[b] Key Laboratory for Special Functional Materials of Ministry of Education, School of Materials and Engineering, Henan University, Kaifeng 475004, China
[c] Department of Physics and Astronomy, University of Waterloo, 200 University Ave, Waterloo, ON, Canada
[d] Department of Electrical and Computer Engineering, University of Toronto, 10 King's College Road, Toronto M5S 3G4, ON, Canada
[e] Department of Chemical Engineering and Applied Chemistry, University of Toronto, Toronto M5S 3E5, ON, Canada
[f] Advanced Photonics Center, School of Electronic Science and Engineering, Southeast University, Nanjing 210096, PR China
[g] Department of Electrical and Computer Engineering, University of Waterloo, 200 University Ave, Waterloo, ON, Canada
[h] School of Physics and Electronics, Henan University, No. 1 Jinming street, Kaifeng, Henan, PR China

ARTICLE INFO

ABSTRACT

Developing highly piezoelectric nanoparticles (NPs) with inherent mechanical-electrical coupling effect is critically important for energy harvesters, self-powered sensors and actuators. Over the past decades, the NPs with a high longitudinal piezoelectric coefficient (d_{33}) were developed for piezoelectric nanogenerators (PENGs) that operate under periodic vertical compression mode. As an alternative, high-performance PENGs can be developed by taking advantage of materials with a superior transverse piezoelectric coefficient (d_{31}). In this work, we successfully synthesized an organic-inorganic hybrid perovskite (OIHP) nanorods (NRs) of (4-amino-tetrahydropyran)$_2$ PbBr$_2$Cl$_2$ [(ATHP)$_2$PbBr$_2$Cl$_2$] that exhibits a large d_{31} of 64.2 pC/N, which is 3 times higher than the well-known poly (vinylidene fluoride) (PVDF) polymer (21 pC/N). A saturated polarization of 5.4 μC/cm^2 and a piezoelectric voltage coefficient (g_{33}) of 900 mV•m/N are also reported. The (ATHP)$_2$PbBr$_2$Cl$_2$ NRs can be dispersed homogeneously in a polymer matrix to make piezoelectric composite films. Due to their excellent flexibility, uniform dispersion and large surface area the concurrent vertical strain and lateral bending yield a high piezoelectric performance. We fabricate a unique piezoelectric composite film for PENGs, which can produce an output voltage (V_{oc}) of 90 V and a short-circuit current (I_{sc}) of 6.5 μA under an applied force of only 4.2 N, outperforming a number of the state-of-the-art PENGs (Table S2). The harvested electrical energy is stored in a capacitor by a two-stage energy transfer mechanism for self-powered electronics. This is the first work, that not only reveals the large transverse piezoelectricity in the (ATHP)$_2$PbBr$_2$Cl$_2$ NRs, but also coins a route to employ it in practical energy harvesting devices.

1. Introduction

Piezoelectric nanogenerators (PENGs), which can convert mechanical energies into electricity, have been considered as a promising energy harvesting tool for self-powered small-sized electronics [1–3]. Since the first manifestation of PENGs based on ZnO nanowires in 2006 [4], great efforts have been devoted to the quest for new piezoelectric materials with larger piezoelectric coefficients [5–7]. In the piezoelectric crystals,

the variation in the electric dipole moment is originated from the applied compressive or torsional mechanical stress. Under uniaxial compression, the induced dipole moment can be parallel or perpendicular to the compressive stress, which is called longitudinal or transverse piezoelectric effects, respectively. In other words, from the analogy of inverse piezoelectric effects-the piezoelectric coefficients d_{33} and d_{31} fundamentally quantifying the efficacy of piezoelectric material are the measure of the deformation of a material in a parallel and perpendicular

direction, respectively, regarding an applied electric field. Due to their high d_{33} value, perovskite-type ceramics (ABX$_3$; A is the cations, B the anions, X the halogens), such as BaTiO$_3$ (BTO), PbTiO$_3$ (PT), and Pb (Zr, Ti) O$_3$ (PZT), are the most widely explored piezoelectric materials for the PENG applications [8–10]. Unfortunately, these highly piezoelectric inorganic ceramics are inherently brittle and their synthesis is often associated with very high temperatures.

In recent decades, as a promising alternative to inorganic ceramics, organic-inorganic hybrid perovskites conjoin the benefits of an organic molecule and inorganic crystal at the molecular level. Besides their distinct optical and electronic properties, the OIHPs are highly desirable for their structural tunability, mechanical flexibility, and low-temperature solution-based process [11–13]. In 2015, Kim et al. firstly employed the OIHPs of MAPbI$_3$ as the piezoelectric centers for the PENGs [14]. Successively, a series of piezoelectric composite films with improved flexibility and durability were achieved via incorporating perovskite NPs in a soft polymer, including FAPbBr$_3$, Fe-doped MAPbI$_3$, and FASnI$_3$ [15–20].

Atomically-thin layered two-dimensional (2D) Ruddlesden-Popper (RP) piezoelectric OIHPs, such as (PMA)$_2$PbX$_4$, (CHA)$_2$PbX$_4$ and (ATHP)$_2$PbX$_4$, have emerged from the shadows of the above ABX$_3$ type perovskites and are expected to have numerous applications in the next generation smart electronics and sensors [21–24]. Previous studies have revealed the 2D piezoelectric OIHPs films can rival or exceed inorganic ferroelectrics in performance, such as high piezoelectric voltage coefficient, large piezoelectric response, and high spontaneous polarization. For instance-(ATHP)$_2$PbX$_4$ film exhibited a giant piezoelectric voltage co-efficient (g$_{33}$) of 660.3 × 10^{-3} mV•m/N, and a high d$_{33}$ of 76 pC/N;

(CHA)$_2$PbX$_4$ possess a high saturated polarization charge density (P$_s$) of 5.8 μC/cm^2. It has been reported that a one-dimensional ferroelectric thin film of DMAACdCl$_3$ has a large d$_{31}$ coefficient of 41 pC/N and a multiaxial ferroelectric thin film of TMBM-MnBr$_3$ demonstrates a large d$_{33}$ of 112 pC/N along its polar axis [25,26]. Even though the excellent piezoelectric performance was reported, however, during the fabrication of an efficient nanogenerator, the pristine 2D OIHP thin films still possess similar brittleness and inflexibility issues as the inorganic piezoelectric materials; hence inhibiting its practical applications where it endures a repeated cycle of mechanical vibration. Moreover, its complex synthesis approach makes it incompatible to be incorporated with the polymer materials for fabricating a high-quality piezoelectric composite film. In this work, we have synthesized novel piezoelectric NRs of (ATHP)$_2$PbBr$_2$Cl$_2$ for a composite film based PENGs integration, where the piezoelectric performance from the NRs is mainly attributed to their transverse piezoelectric coefficient d$_{31}$ rather than d$_{33}$. Inter-estingly these NRs have a longer length, which is suitable for bending during applied mechanical stress, and it has excellent dissolvability in polymer to fabricate composite piezoelectric films. Benefitting from this superior transverse piezoelectricity of the NRs we demonstrate a high-performance flexible PENG for self-powered electronics.

Non-piezoelectric 2D perovskite nanomaterials can typically be synthesized at room temperature by using a ligand-assisted reprecipitation (LARP) technique [27,28]. In this paper, we adopt a modified LARP technique [29] and successfully synthesize the piezoelectric NRs of (ATHP)$_2$PbBr$_2$Cl$_2$ at room temperature. The crystal structure of (ATHP)$_2$PbBr$_2$Cl$_2$ has an RP layered stacking, in which the amine groups of ATHP are bonded to the PbX$_6$ (X is Cl or Br) octahedrons by hydrogen
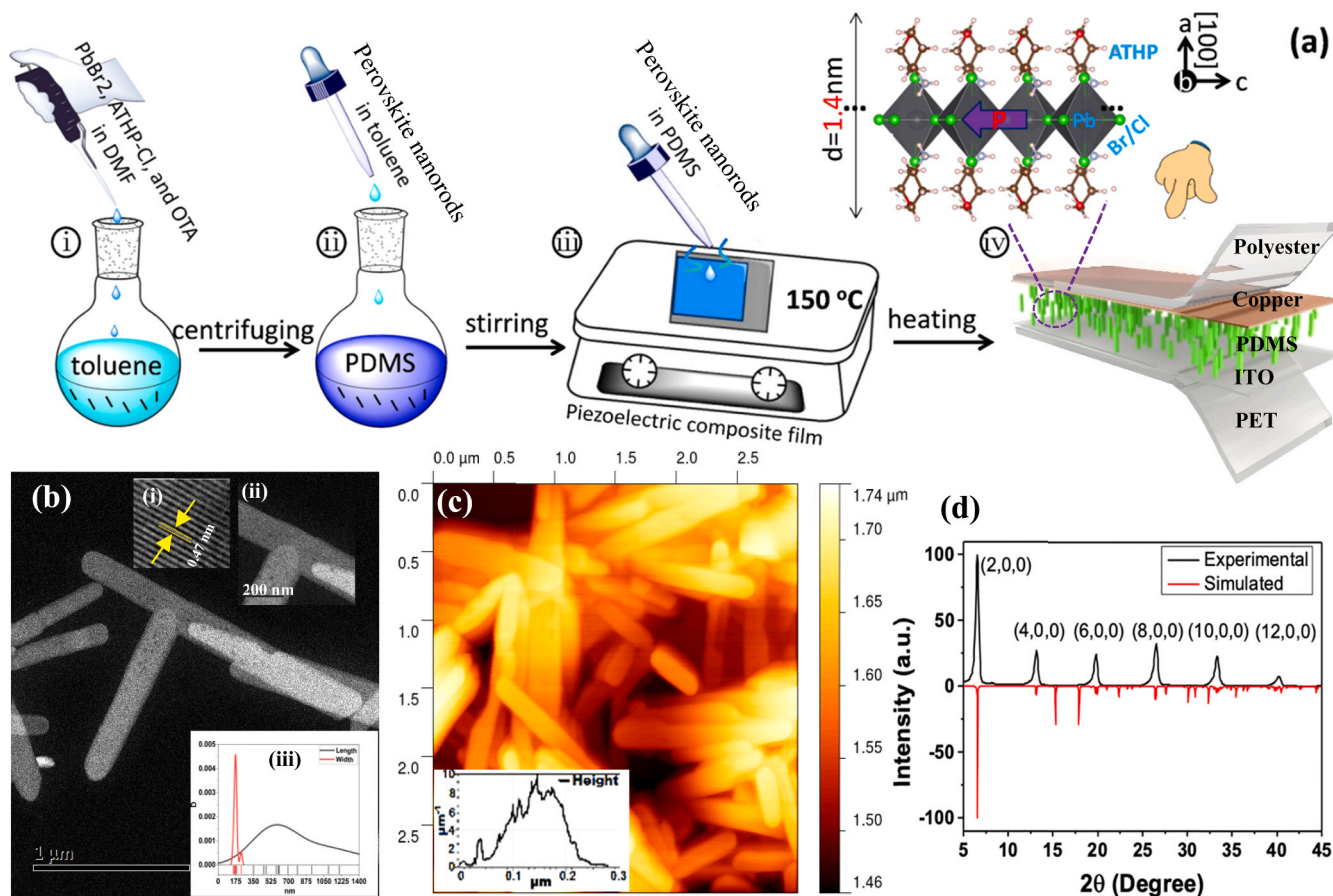
Fig. 1. (a) sketch of the synthesis process of (ATHP)$_2$PbBr$_2$Cl$_2$ NRs (i) the growth of composite films (ii and iii) and the fabrication of PENGs (iv); (b) TEM and (c) AFM images of the (ATHP)$_2$PbBr$_2$Cl$_2$ NRs. Insets: (b) close-in view (i-ii) of nanorods (iii) length and width distribution; (c) thickness distribution of the as-synthesized (ATHP)$_2$PbBr$_2$Cl$_2$ NRs; (d) experimental (black) and simulated (red) XRD patterns of the (ATHP)$_2$PbBr$_2$Cl$_2$ NRs film. The (ATHP)$_2$PbBr$_2$Cl$_2$ NRs film gives sharp periodic (200) planar peaks in the XRD pattern denoting [100] orientation.

bonding interaction and the oxygen (O) atoms remain outwards (Fig. 1a) [24]. Using state-of-the-art piezo response force microscopy (PFM), we show that the synthesized $(ATHP)_2PbBr_2Cl_2$ NRs exhibit a superior d_{31} of 64.2 pC/N which is ~ 3-times higher than the commonly used piezoelectric PVDF polymer. By dispersing these NRs into a poly-dimethylsiloxane (PDMS) polymer matrix, a homogeneous and chemically stable piezoelectric composite film of $(ATHP)_2PbBr_2Cl_2$@PDMS was achieved where a vertical strain and lateral bending of the NRs are observed due to its higher surface stress and improved flexibility, confirmed through finite element simulation. Finally, benefited from the synergistic contribution from material piezoelectric coefficients of both d_{31} and d_{33}, PENGs based on the synthesized $(ATHP)_2PbBr_2Cl_2$@PDMS composite film produces a piezoelectric output voltage (V_{oc}) of 90 V, short-circuit current (I_{sc}) of 6.5 μA, and a power density of 1.7 μW/cm^2, under a small periodic compressing force of 4.2 N (4.66 kPa). This output-power density is higher than the previously reported Sm-PMN-PT@PDMS, FAPbBr$_3$@PDMS, and BaTiO$_3$@PDMS composite film based PENGs in Table S2, which are 11.5 μW/cm^2 (at 0.35 MPa), 12 μW/cm^2 (at 0.5 MPa), and 0.12 μW/cm^2 (at 0.002 MPa), respectively. The harvested electrical energy is collected and stored by an energy-efficient two-stage charge transfer system. This study on synthesizing the $(ATHP)_2PbBr_2Cl_2$ NRs and revealing its transverse piezoelectricity will innovatively enrich the versatility of OIHP ferroelectrics and promote their burgeoning potentialities to be used as the active material for next-generation PENGs applications.

2. Results and discussion

The fabrication processes of the PENGs based on $(ATHP)_2PbBr_2Cl_2$ NRs are consecutively illustrated in Fig. 1a: (i) $(ATHP)_2PbBr_2Cl_2$ NRs are synthesized via the LARP technique (more details are in the experimental section of the Supporting Information). (ii) Piezoelectric composite precursor is prepared via dispersing the $(ATHP)_2PbBr_2Cl_2$ NRs into PDMS; (iii) A piezoelectric composite film is formed by drop-casting the step-ii precursor onto a polyethylene terephthalate (PET) substrate coated with a conductive indium tin oxide (ITO) and then curing the solution at 150 °C for 40 min; (iv) Then a copper (Cu) tape is attached to the top surface of the OIHP piezoelectric composite film as a top electrode and then a high electrical poling voltage of 6.0 kV is applied between the electrodes for 2–3 h to align the piezoelectric dipoles of the film (more details are in the fabrication method of the Supporting Information). Finally, the device was thermally laminated with a top polyester substrate (Fig. 1a (iv)).

The morphology of the $(ATHP)_2PbBr_2Cl_2$ NRs is studied via transmission electron microscopy (TEM), atomic force microscopy (AFM), and X-ray diffraction pattern (XRD). For the TEM and AFM experiments, the samples are prepared via dipping the diluted NPs solution (Fig. S1) onto a clean and smooth surface (average roughness < 1 nm) of a silicon wafer (AFM topography image in Fig. S2). From the high-resolution TEM image of the distinct NRs in Fig. 1b, the lattice spacing was measured to be 0.47 nm (inset i), which matches the (200) facet of the perovskite structure. The close-in view of the nanorod width obtained from the TEM image is also shown in Fig. 1b (inset ii). From the histogram representation (inset iii) demonstrating the length and width distribution of the NRs, the average length of the nanorods was 771.3 nm with a minimum of 351.8 nm, and a maximum of 1480 nm. The average width was 175.65 nm with a minimum of 151.2 nm and a maximum of 227.8 nm. The thickness of as-synthesized NRs is confirmed by the AFM in Fig. 1c. From the AFM, the thicknesses of the NRs ranges were measured from 100 to 200 nm. (see the inset height distribution in Fig. 1c). The TEM and AFM images (Fig. 1b and c) confirm the formation of the NRs of $(ATHP)_2PbBr_2Cl_2$ crystal (crystal structure in Fig. S3). The phase purity of the NR film was confirmed by the infrared (IR) spectroscopy (Fig. S4). Compared with the simulated XRD in Fig. 1d, the measured XRD of the $(ATHP)_2PbBr_2Cl_2$ NRs film on silicon only exhibits sharp (l00) planar peaks (l = 2, 4, 6, 8, 10, 12), suggesting that the NRs

are mostly oriented in the [100] direction [29]. To determine the phase transition of the $(ATHP)_2PbBr_2Cl_2$ NRs film, differential scanning calorimetry (DSC) measurements were performed (Fig. S5). Two pairs of reversible peaks at 219/236 °C and 197/213 °C (heating/cooling) were observed indicating that the compound had two phase transitions at T_1 = 219 °C and T_2 = 236 °C. The high $T_{1,2}$ of the compound is expected due to the short distance between octahedral PbBr$_2$Cl$_2$ layers as compared to other perovskites, leading to a more compact crystal structure and thus restricts its cations movements [24]. The two reversible transitions may be due to the conversion of the compound at T_1 to its coordination isomer with a modified crystalline packing and a different distance between the Pb atoms in adjacent chains [30].

The piezoelectric polarization in the $(ATHP)_2PbBr_2Cl_2$ NRs is examined via the lateral (transverse) (Fig. 2a) and vertical (longitudinal) PFM methods (Fig. 2b). In the lateral PFM measurements (L-PFM), in-plane displacement (laser deflection in the x-axis) arises from the shear strain between the PFM cantilever tip and the sample (Fig. 2a). To probe the PFM cantilever tip a sequence of direct current (dc) voltages from −10 to 10 V with a superimposed alternating current (ac) voltage of 2 V was applied. In principle, the electric domain forms in the ferroelectric material can be switched by an external electric field. Due to the inherent polarization switching characteristics, and remnant polarization phenomena at zero bias, the sequential application of an electric field to the ferroelectric material generate a phase loop and a butterfly-shaped amplitude loop in the PFM measurement. During the transverse piezo response measurements (L-PFM), the phase-hysteresis loop exhibits a 180° change (inset in Fig. 2c) and the amplitude curve in Fig. 2c shows a characteristic butterfly feature. The L-PFM is a strong indicator of the in-plane transverse piezo response produced by the in-plane polarization in the $(ATHP)_2PbBr_2Cl_2$ NRs [25]. During the L-PFM measurements, the deformation of the sample is perpendicular to the cantilever motion and deformation-amplitude varies proportionally with the applied voltage.

To determine the d_{31} in the $(ATHP)_2PbBr_2Cl_2$ NRs, we used a standard poled PVDF film (Polyk Technologies, USA) as a benchmark in the L-PFM measurements, whereas the tip-cantilever was aligned perpendicular to the a-axis of the PVDF. As shown in Fig. 2d, the slope of the measured L-PFM amplitude vs. drive voltage curve of $(ATHP)_2PbBr_2Cl_2$ (K_1 = 0.12) is almost 3 times that of the reference PVDF sample (K_2 = 0.04) [31]. Therefore, the d_{31} of $(ATHP)_2PbBr_2Cl_2$ should be ~64 pC/N, which is rather competitive in comparison to traditional perovskites and other molecular materials listed in Table S1.

Then the ferroelectric domain pattern of the $(ATHP)_2PbBr_2Cl_2$ in the lateral mode was investigated in Fig. 2e–g. There was a clear contrast in the lateral amplitude and phase (−180° to 180°) images in Fig. 2f and g (small noises are present due to the lower bias voltage of 3.6 V). The minimum signal values in the amplitude image (Fig. 2f) are the domain walls separating the adjacent domains. This evidence of domains is the indication of in-plane ferroelectricity in the $(ATHP)_2PbBr_2Cl_2$ NRs. In contrast, out-of-plane deformation (laser deflection in the y-axis) from the sample is estimated from the vertical bending motion of the tip during the vertical PFM (longitudinal) measurements. The vertical PFM (V-PFM) measurements does not exhibit a measurable phase change in Fig. S6c, and the piezo response amplitude contrast (Fig. S6b) was weaker than the L-PFM measurements. The results exclude the out-of-plane polarization, rather it is predominantly occurring in the transverse direction-(100) plane of the $(ATHP)_2PbBr_2Cl_2$ NRs, which is consistent with the previously reported work [25]. This superior polarization in the transverse direction is yielding higher piezoelectric coefficient (d_{31}). Similarly, we observed ferroelectric domain patterns of an externally poled PVDF sample (Fig. S7). The sample was attached on an FTO/glass substrate by using conductive silver (Ag) paste. The domain patterns were visible in both L-PFM and V-PFM images, indicating that both in-plane and vertical polarization components contributed to the total ferroelectric polarization. The piezo response signal strength (Fig. S7d-e) at the vertical polarization direction for the
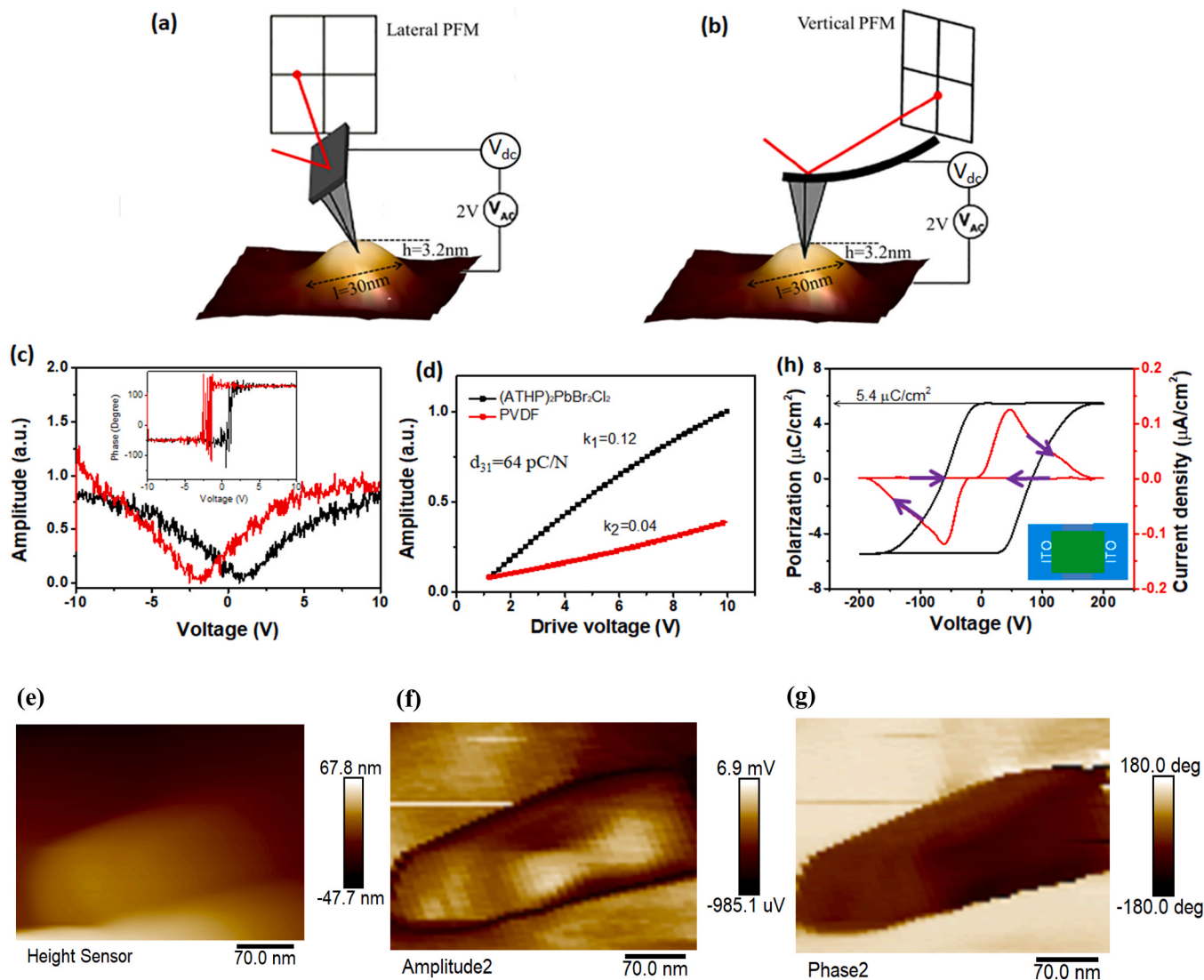
Fig. 2. Origin of piezoelectricity from the $(ATHP)_2PbBr_2Cl_2$ NRs: (a) a schematic representation of lateral (a) and vertical (b) PFM methods; (c) local lateral (transverse) piezoelectric response amplitude and phase hysteresis (inset) versus cyclic direct current (dc) voltage loops from −10 to 10 V; (d) comparison of the lateral PFM resonance amplitude of the $(ATHP)_2PbBr_2Cl_2$ NR and a commercial poled PVDF film; (e) surface topography (f) lateral PFM amplitude and (g) phase images of the $(ATHP)_2PbBr_2Cl_2$ NRs (h) current density-voltage (J-V) curve and the integrated polarization-voltage (P-V) hysteresis loop of the $(ATHP)_2PbBr_2Cl_2$ film at room temperature (25 °C) obtained by using the double-wave method.

PVDF was presumably to be the highest, however, the higher thickness of the film ("10 μm) was limiting the piezo response in the vertical direction with a maximum applied voltage range of up to 10 V. The phase image during the L-PFM of the PVDF (Fig. S7c) exhibited an excellent contrast and varied from −263.7° to 263.2°, whereas in the V-PFM (Fig. S7e) it was within −150.5° to −134.7°. It should be noted that the piezoelectric response from the PFM techniques may contain long-range electrostatic interactions and non-local interactions between the tip and sample surface [32]. Therefore we performed kelvin probe force microscopy (KPFM) on the surface of the $(ATHP)_2PbBr_2Cl_2$ (Fig. S8) NRs. Since the surface topography in the KPFM does not exhibit any patterns as found in the PFM images; we exclude any significant influence of the topography on the domain patterns [33]. The homogeneous surface-potential distribution on the surface of the $(ATHP)_2PbBr_2Cl_2$ in Fig. S8b rules out any contributions from the domains. Rounded surfaces and angled crystal flanks may result in a change of the surface potential due to the deviation of crystal faces from the three main faces of the

perovskites [33]. However, a small deviation in the average surface potential (~200 mV) eliminates the major effects of any noteworthy remnant precursors on the surface (Fig. S8c and d).

The polarization switching behavior at room temperature can also be observed by measuring the current density-voltage (J-V) curve and polarization-voltage (P-V) hysteresis loop. For this measurement, a sample is prepared by drop-casting and curing the NRs film between two ITO electrodes (the inset in Fig. 2h). As shown in Fig. 2h, two peaks with opposite signs in the J-V curve are observed at ±50 V, revealing two stable states with opposite polarization. The saturated polarization (P_s) is estimated from the P-V hysteresis loop to be 5.4 μC/cm², which is close to the previously reported value of 5.6 μC/cm² for the bulk $(ATHP)_2PbBr_4$ [24].

To explore the practical energy harvesting performance of the $(ATHP)_2PbBr_2Cl_2$ NRs, the PENGs are fabricated by using the OIHP composite film as the piezoelectric layer. Fig. 3a shows the cross-sectional scanning electron microscopy (SEM) image of a fabricated
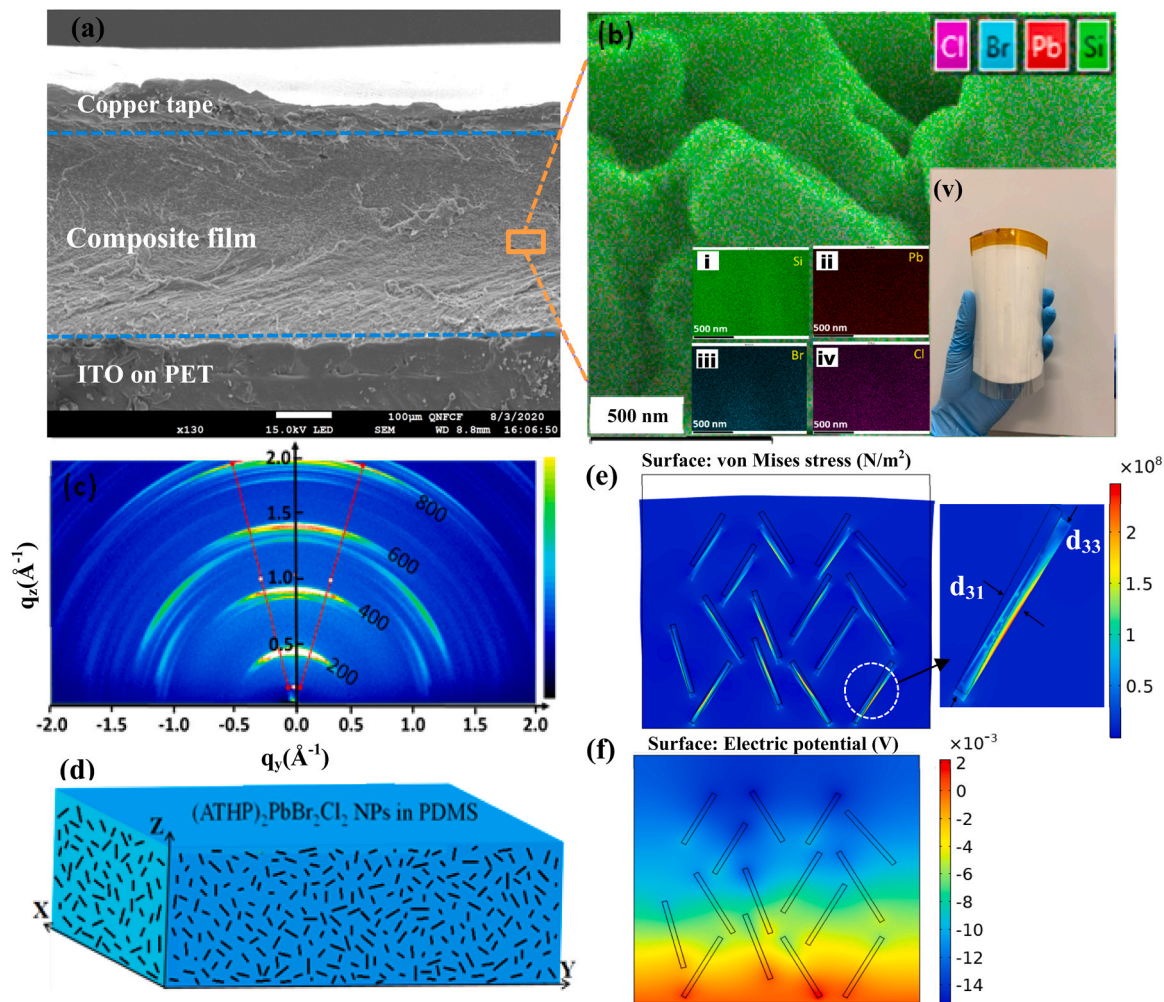
Fig. 3. Morphology of (ATHP)$_2$PbBr$_2$Cl$_2$ NRs @PDMS composite films: (a) the cross-sectional SEM and (b) SEM-EDS mapping images of spin-coated 30 wt% (ATHP)$_2$PbBr$_2$Cl$_2$ NRs @PDMS composite films on ITO/FTO substrate (inset shows (i-iv) elemental mapping of Si, Pb, Br, and Cl, respectively in the PDMS; and (v) a large area PENG device); (c) GIWAXS image for 30 wt% (ATHP)$_2$PbBr$_2$Cl$_2$ NRs @PDMS composite films (d) schematic illustration of the orientation of (ATHP)$_2$PbBr$_2$Cl$_2$ NRs in PDMS; (e and f) finite element simulation of the composite films by COMSOL Multiphysics (the rod-like structure of the nanoparticles were approximated from the TEM and AFM images in Fig. 1b and c), demonstrating (e) stress distribution (inset shows the close-in view of a single nanorods with higher bending stress) and (f) electric potential distribution.

PENG. It can be seen that the piezoelectric composite film loaded with 30 wt% (ATHP)$_2$PbBr$_2$Cl$_2$ has a thickness of about ~300 μm and is sandwiched uniformly between a top copper electrode and a bottom ITO-coated PET substrate. Fig. 3b is a zoomed-in SEM energy dispersive spectroscopy (EDS) mapping over the cross-section of the fabricated PENGs device (elemental mappings of Si, Pb, Br, and Cl in the insets (i-iv), and a fabricated device photo is shown in the inset (v) of Fig. 3b). From the SEM-EDS images in Fig. 3b, it is clear that the (ATHP)$_2$PbBr$_2$Cl$_2$ NPs (corresponding to the elemental mapping of Br, Cl, and Pb) are dispersed homogeneously in the PDMS (corresponding mapping of Si) matrix. The uniform dispersion of the NPs in the composite film is critical to obtain optimum piezoelectric performance, as the NPs will act as the mechanical load- carrying center and homogeneous NPs distribution will increase the high voltage poling breakdown-strength of the film.

The orientation of polarization in the NRs is important for the piezoelectric performance as elucidated in the earlier studies of 2D MoS$_2$-based PENGs [34–36]. From the grazing-incidence wide-angle X-ray scattering (GIWAXS) of the (ATHP)$_2$PbBr$_2$Cl$_2$@PDMS composite film in Fig. 3c, quasi-Debye-Scherrer rings are observed, which is

expected due to the random orientation of the NRs (Fig. 3d). This is different from the reported 2D perovskite quantum wells orientation-where the polarization is perpendicular to the vertical compression [37]. This phenomenal discrepancy should be attributed to supporting the flexible NRs by the PDMS scaffold.

Based on the orientational evidence from the GIWAXS, the finite element simulation is performed to explore the origin of high piezo-electric potential for this composite film structure. The simulation results are shown in Fig. 3e and f. The random orientation of the NRs in the composite film is found to generate an effective static potential along the vertical strain direction. As the NRs are supported by the polymer scaffold, the compressive stress will eventually induce an effective bending moment on them (stress distribution in Fig. 3e). Besides the vertical strain, due to its flexible rod-like feature much higher lateral bending in the NRs can synergistically enhance device piezoelectric performance. Therefore, the resulting piezoelectric potential in the composite film in Fig. 3f can be attributed to the combined contribution from their d$_{33}$ and d$_{31}$ coefficients (or the effective d$_{33}$), in which the d$_{31}$ plays a dominant role. The finite element simulation was further extended in Figs. S9 and S10, where the generated piezoelectric

potential from a single nanorod (width and height of 100 nm and 450 nm) was calculated and compared with a thin film structure of the same size. With the applied pressure of 100 N/m^2, the stress and electric potential were computed in the direction both perpendicular (Fig. S9e and f), and parallel (Fig. S9g and h) to the applied pressure. From the finite element calculation, the nanorod with a high aspect ratio structure generating potential in the transverse direction due to its induced tensile and compressive stress in its two sides; the stress is, however, asymmetric and depends on the orientation of the nanorods. Subsequently, the induced potential in the nanorod was compared to the thin film with a pressure range from 0 to 100 N/m^2 (Fig. S10). From the slope of the induced potential to the applied pressure, the calculated piezo response corresponding to the effective piezoelectric voltage coefficient (g$_{33}$*) was ~4-times higher in the nanorod; therefore, such nanorods could be valuable for designing efficient PENGs.

The piezoelectric output of the PENGs is measured by mounting the test device on an electrodynamic shaker, which goes through a period-ical vertical compressing and releasing process (characterization set-up in Fig. S11). According to the equation of short-circuit current density J$_{sc}$ = (d$_{33}$* × ΔP)/Δt, (where d$_{33}$* is the effective piezoelectric coefficient of the composite film, ΔP is applied pressure, and Δt is time) the output J$_{sc}$ is proportional to the d$_{33}$* [15]. Fig. 4a shows that the measured d$_{33}$* of a pure PDMS film is close to zero, which implies that the measured d$_{33}$* value of the composite films is mainly attributed to the addition of the (ATHP)$_2$PbBr$_2$Cl$_2$ NRs. When the mass ratio of embedded NRs in the PDMS matrix increases from 10 to 40 wt%, the d$_{33}$* value of the composite film linearly increases from 19 to 56 pC/N, which was measured by a quasi-static d$_{33}$ meter. It is experimentally found that the mass ratio of the NRs in the PDMS beyond 40 wt% is rather difficult for thermal curing hence to fabricate a practical device. Note that the highest d$_{33}$* of the composite film is two times higher than the commercial poled PVDF (28 pC/N) film. In contrast, the output voltage (V$_{oc}$) is determined by the piezoelectric voltage coefficient (g$_{33}$*) which is defined as (d$_{33}$*/(ε$_0$ × ε$_r$)) and expressed in the unit of mV•m/N. From the equation of V$_{oc}$
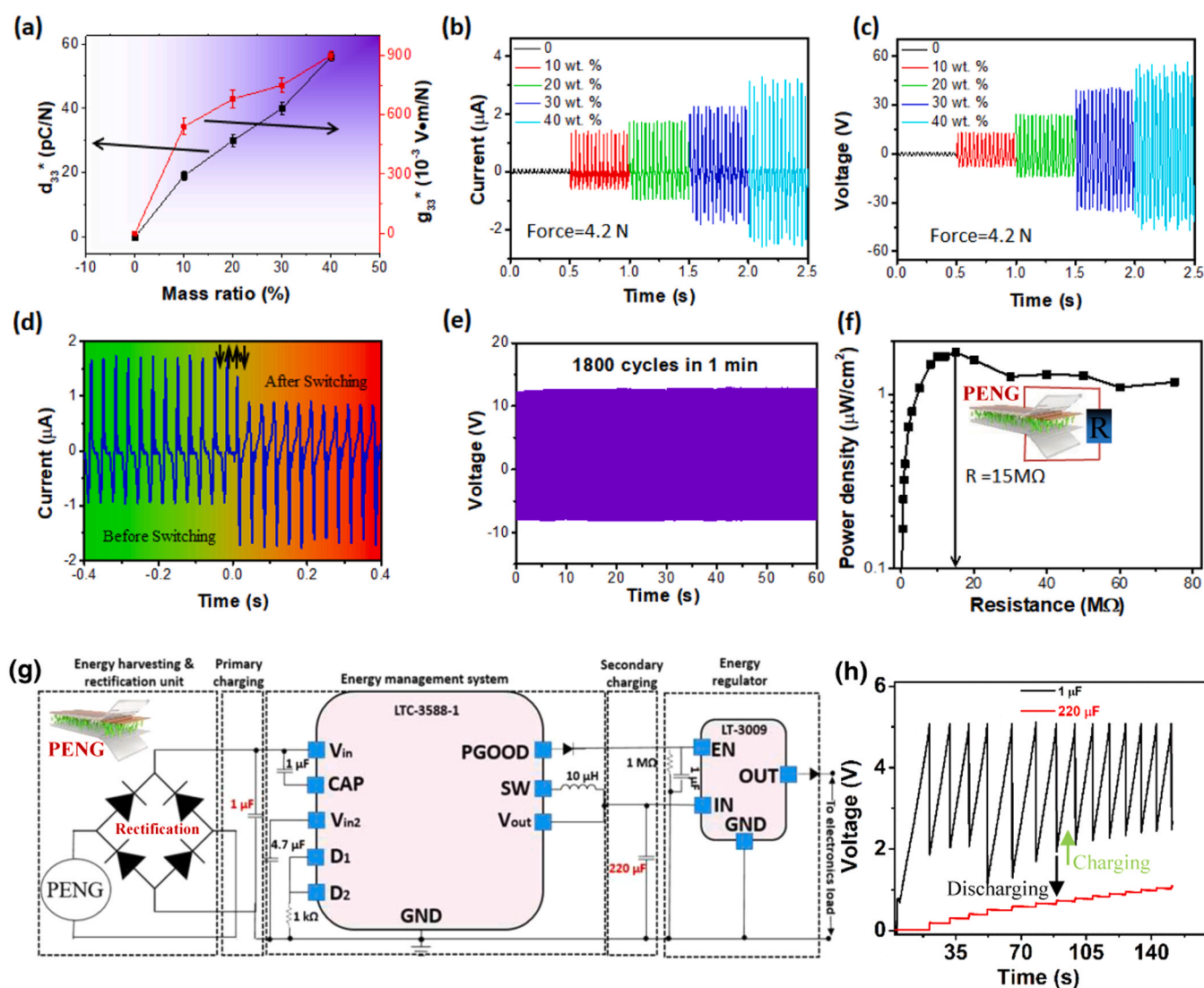
Fig. 4. The output performance of the PENGs: (a) the measured d$_{33}$* and g$_{33}$* for the composite film with different (ATHP)$_2$PbBr$_2$Cl$_2$ concentration; (b) the I$_{sc}$ and (c) V$_{oc}$ of the PENGs with different (ATHP)$_2$PbBr$_2$Cl$_2$ concentration at an applied force of 4.2 N;(d) the polarity switching test of the I$_{sc}$ of the PENG (20 wt%, 4.2 N);(e) reliability testing for 1 min (30 wt% PENGs, 30 Hz, 3.5 N); (f) measured output power-density of the PENGs across various loads from 0 to 75 MΩ (g) block diagram of the two-stage energy management and regulation unit (h) storing the harvested energy to the capacitors; initially small value (1μF) capacitor is charged (black curve) up to 5 V, then the charges are transferred to large value (220 μF) capacitor (red curve) thus completing a single charging cycle.

$= g_{33}{}^* \times \Delta P \times L$, (where L is the original thickness of the composite film) a high output voltage is associated with a high $g_{33}{}^*$ value which is inversely proportional to the relative permittivity (ε_r) [38]. The ε_r of the $(ATHP)_2PbBr_2Cl_2$ film is measured to be ~28–18 at frequencies ranging from 1 kHz to 1 MHz (Fig. S12), which is relatively much smaller than most of the reported highly piezoelectric perovskite ceramics, such as BTO or PZT (having high ε_r value of above hundreds) [39]. The thermal stability of the relative permittivity was also measured for one hour at 130 °C, and 200 kHz for the 30 wt% $(ATHP)_2PbBr_2Cl_2$@PDMS composite film (Fig. S13). The permittivity values measured at every 10 min for 60 min showed a minor variation of ±0.02, due to the highly stable phase of this composite material system, which would be suitable for energy harvesting in harsh environments.

Along with the measured quasi-static (110 Hz, 0.25 N) $d_{33}{}^*$ values of the film, the $g_{33}{}^*$ of the composite films are calculated and plotted in Fig. 4a with the previously measured ε_r values.

Comparing Fig. 4a with c, the rising trend of $g_{33}{}^*$ from 560 to a high value of 900 mV•m/N is consistent with that of the measured high V_{oc} (peak to peak) from 30 to a maximum of 90 V. More specifically, the higher $d_{33}{}^*$ value yields a maximum I_{sc} (peak to peak) of 6.5 µA (Fig. 4b). Notably, the highest $g_{33}{}^*$ of 900 mV•m/N from the 40 wt% $(ATHP)_2PbBr_2Cl_2$@PDMS composite film is ~4 times that of standard piezoelectric PVDF film.

The effect of the poling voltages on the PENG's output was also studied in Fig. S14. The generated output voltages were recorded at 30 Hz for a range of poling voltages from 0 V (non-poled) to 5 kV. The low output voltage (~7 V) from the non-poled PENG device was increased to ~75 V when the device was poled at 5 kV. Typical polarity-switching tests are carried out to validate the outputs originating from the piezoelectric contribution [8,40–42]. The I_{sc} of the PENGs switches its polarity from positive to negative direction during the electrical connection reversal in Fig. 4d, arguably anticipated due to the surface piezoelectric polarization charges. Moreover, a non-symmetrical feature of the I_{sc} value across the x-axis (time) is observed during the experiments, which can be explained by the difference in the strain rate while applying and removing the stress on the PENGs (the detailed working mechanism in Fig. S15). The reliability of the PENGs is explored by continuously testing the device for 1 min (1800 cycles). Throughout the complete time span, no observable degradation (Fig. 4e) in the amplitude of the output voltage is found. Moreover, the stability of the device was assessed for 2 weeks (Fig. S16), which exhibited a small deviation of only ±2 V of its output voltage.

To optimize the maximum power delivered to the loads, the electrical output power of the PENGs is measured as a function of load resistance ranging from 0.09 to 75.4 MΩ (Fig. 4f). The maximum output power density of 1.7 µW/cm² is obtained with an external load resistor of 15 MΩ, and an applied force of 4.2 N. This power density value is well anticipated because the I_{sc} of the PENGs varies proportionally with the applied pressure (Fig. S17) where the power density increases proportionally with the squared of the I_{sc} value. This optimized PENG performance, including the $V_{oc(p-p)}$ of 90 V, $I_{sc(p-p)}$ of 6.5 µA, and power density of 1.7 µW/cm² under an applied force of only 4.2 N, are rather competitive in terms of output power to input mechanical energy comparison to that of previously reported PENGs using the same PDMS matrix (Table S2).

Finally, to store the harvested energy by the PENG, an energy-efficient two-stage charge transfer circuit was designed (Fig. 4g). The output electrical signal from the PENG is rectified by a full-bridge rectifier circuit in the energy harvesting and rectification unit and fed to a small value capacitor (1 µF), which is the primary charging unit. The charging level of the small capacitor (corresponding black charging curve in Fig. 4h) was regulated to a maximum of 5 V by a commercial LTC-3588-1 module. When the output voltage of the small capacitor reaches 5 V, a certain portion of the electrical energy (voltage drop from ~5 V to ~3 V level in Fig. 4h) is transferred to a larger value capacitor (220 µF) in the secondary charging unit (corresponding voltage stepping

up of the red charging curve in Fig. 4h). The charging current in the 220 µF capacitor is ramped up to mA level by an inductor (10 µH) and two built-in MOSFET switches in the LTC-3588-1 module. After the energy discharge from the small value capacitor, the LTC-3588-1 module disconnects the larger capacitor, and then the small capacitor starts charging again. In this periodic manner, generated energy from the harvester can be stored more efficiently in a capacitor (more details are in the Supplementary Note 1). Any electronic or wireless circuits can be repeatedly powered up by this stored energy and thus potentially realizing self-powered wireless sensing [43–47], structural health monitoring, self-powered implantable biomedical devices, etc.

3. Conclusion

In summary, we synthesize OIHP piezoelectric NRs of $(ATHP)_2PbBr_2Cl_2$ and reveal its superior transverse piezoelectricity of 64.2 pC/N (3-times higher than the PVDF), by using the state-of-the-art piezoelectric material characterization tools. From the PFM measurement, the polarization direction in the pristine $(ATHP)_2PbBr_2Cl_2$ NR is found along the [001] direction in the (100) plane. Due to its excellent solubility in the organic solvent, the piezoelectric composite film was prepared via dispersing the $(ATHP)_2PbBr_2Cl_2$ NRs in the PDMS. The energy dispersive X-ray elemental mapping and GIWAXS characterizations unfolded the uniform and spontaneous distribution of the NRs in the PDMS matrix. Benefiting from the improved flexibility and a rod-like nanostructure with a large surface area, the transverse piezoelectricity contributes greatly to the piezoelectric potential of the composite film. The fabricated devices show the highest outputs with the V_{oc} of 90 V, I_{sc} of 6.5 µA, and a power density of 1.7 µW/cm² with an applied force of only 4.2 N, signifying successful manufacturing of an efficient PENG. The energy generated by the PENG was successfully collected by an efficient two-stage energy transfer mechanism and stored in a capacitor for self-powered electronics integration of the PENGs. It is anticipated that the piezoelectric performance of these NRs can be significantly improved further to realize a highly efficient piezoelectric nanogenerator for the next generation sensing and actuating applications.

CRediT authorship contribution statement

Asif Abdullah Khan: Conceptualization, Methodology, Investigation, Data curation, Formal analysis, Writing - original draft. **Guangguang Huang:** Conceptualization, Methodology, Investigation, Data curation, Formal analysis, Writing - original draft. **Md. Masud Rana:** Investigation, Data curation, Formal analysis. **Nanqin Mei:** Investigation. **Margherita Biondi:** Investigation. **Shazzad Rassel:** Investigation. **Nicolas Tanguy:** Investigation, Data curation. **Bin Sun:** Investigation, Reviewing. **Zoya Leonenko:** Supervision, Reviewing. **Ning Yan:** Supervision, Reviewing. **Chunlei Wang:** Supervision. **Shuhong Xu:** Supervision. **Dayan Ban:** Conceptualization, Methodology, Data curation, Writing - review & editing, Supervision.

Declaration of Competing Interest

The authors declare that they have no known competing financial interests or personal relationships that could have appeared to influence the work reported in this paper.

Appendix A. Supporting information

Supplementary data associated with this article can be found in the online version at doi:10.1016/j.nanoen.2021.106039.

References

[1] C. Pan, J. Zhai, Z.L. Wang, Piezotronics and piezo-phototronics of third generation semiconductor nanowires, Chem. Rev. 119 (2019) 9303–9359.

[2] C.R. Bowen, H.A. Kim, P.M. Weaver, S. Dunn, Piezoelectric and ferroelectric materials and structures for energy harvesting applications, Energy Environ. Sci. 7 (2014) 25–44.

[3] Z.L. Wang, On the first principle theory of nanogenerators from Maxwell's equations, Nano Energy 68 (2020), 104272.

[4] Z.L. Wang, J. Song, Piezoelectric nanogenerators based on zinc oxide nanowire arrays, Science 312 (2006) 242–246.

[5] M.-H. Zhao, Z.-L. Wang, S.X. Mao, Piezoelectric characterization of individual zinc oxide nanobelt probed by piezoresponse force microscope, Nano Lett. 4 (2004) 587–590.

A. Mahmud, A.A. Khan, P. Voss, T. Das, E. Abdel-Rahman, D. Ban, A high performance and consolidated piezoelectric energy harvester based on 1D/2D hybrid zinc oxide nanostructures, Adv. Mater. Interfaces 5 (2018), 1801167.

[7] S. Xu, Y. Qin, C. Xu, Y. Wei, R. Yang, Z.L. Wang, Self-powered nanowire devices, Nat. Nanotechnol. 5 (2010) 366–373.

[8] X. Niu, W. Jia, S. Qian, J. Zhu, J. Zhang, X. Hou, J. Mu, W. Geng, J. Cho, J. He, X. Chou, High-performance PZT-based stretchable piezoelectric nanogenerator, ACS Sustain. Chem. Eng. 7 (2018) 979–985.

[9] N.R. Alluri, A. Chandrasekhar, V. Vivekananthan, Y. Purusothaman, S. Selvarajan, J.H. Jeong, S.-J. Kim, Scavenging biomechanical energy using high-performance, flexible BaTiO3 nanocube/PDMS composite films, ACS Sustain. Chem. Eng. 5 (2017) 4730–4738.

[10] K.Y. Lee, D. Kim, J.-H. Lee, T.Y. Kim, M.K. Gupta, S.-W. Kim, Unidirectional high-power generation via stress-induced dipole alignment from ZnSnO3 nanocubes/polymer hybrid piezoelectric nanogenerator, Adv. Funct. Mater. 24 (2014) 37–43.

[11] W. Li, Z. Wang, F. Deschler, S. Gao, R.H. Friend, A.K. Cheetham, Chemically diverse and multifunctional hybrid organic–inorganic perovskites, Nat. Rev. Mater. 2 (2017) 16099.

[12] G. Huang, C. Wang, H. Zhang, S. Xu, Q. Xu, Y. Cui, Post-healing of defects: an alternative way for passivation of carbon-based mesoscopic perovskite solar cellsviahydrophobic ligand coordination, J. Mater. Chem. A 6 (2018) 2449–2455.

[13] Y. Li, X. Zhang, H. Huang, S.V. Kershaw, A.L. Rogach, Advances in metal halide perovskite nanocrystals: synthetic strategies, growth mechanisms, and optoelectronic applications, Mater. Today 32 (2020) 204–221.

[14] Y.-J. Kim, T.-V. Dang, H.-J. Choi, B.-J. Park, J.-H. Eom, H.-A. Song, D. Seol, Y. Kim, S.-H. Shin, J. Nah, S.-G. Yoon, Piezoelectric properties of CH3NH3PbI3 perovskite thin films and their applications in piezoelectric generators, J. Mater. Chem. A 4 (2016) 756–763.

[15] R. Ding, H. Liu, X. Zhang, J. Xiao, R. Kishor, H. Sun, B. Zhu, G. Chen, F. Gao, X. Feng, J. Chen, X. Chen, X. Sun, Y. Zheng, Flexible piezoelectric nanocomposite generators based on formamidinium lead halide perovskite nanoparticles, Adv. Funct. Mater. 26 (2016) 7708–7716.

[16] R. Ding, X. Zhang, G. Chen, H. Wang, R. Kishor, J. Xiao, F. Gao, K. Zeng, X. Chen, X. W. Sun, Y. Zheng, High-performance piezoelectric nanogenerators composed of formamidinium lead halide perovskite nanoparticles and poly (vinylidene fluoride), Nano Energy 37 (2017) 126–135.

[17] V. Jella, S. Ippili, J.-H. Eom, J. Choi, S.-G. Yoon, Enhanced output performance of a flexible piezoelectric energy harvester based on stable MAPbI3-PVDF composite films, Nano Energy 53 (2018) 46–56.

[18] A.A. Khan, M.M. Rana, G. Huang, N. Mei, R. Saritas, B. Wen, S. Zhang, P. Voss, E.-A. Rahman, Z. Leonenko, S. Islam, D. Ban, Maximizing piezoelectricity by self-assembled highly porous perovskite–polymer composite films to enable the internet of things, J. Mater. Chem. A 8 (2020) 13619–13629.

[19] R. Pandey, G. Sb, S. Grover, S.K. Singh, A. Kadam, S. Ogale, U.V. Waghmare, V. R. Rao, D. Kabra, Microscopic origin of piezoelectricity in lead-free halide perovskite: application in nanogenerator design, ACS Energy Lett. 4 (2019) 1004–1011.

[20] S. Ippili, V. Jella, J. Kim, S. Hong, S.-G. Yoon, Enhanced piezoelectric output performance via control of dielectrics in Fe^{2+}-incorporated MAPbI3 perovskite thin films: flexible piezoelectric generators, Nano Energy 49 (2018) 247–256.

[21] X. Gao, J. Wu, Y. Yu, Z. Chu, H. Shi, S. Dong, Giant piezoelectric coefficients in relaxor piezoelectric ceramic PNN-PZT for vibration energy harvesting, Adv. Funct. Mater. 28 (2018), 1706895.

[22] H.Y. Ye, W.Q. Liao, C.L. Hu, Y. Zhang, Y.M. You, J.G. Mao, P.F. Li, R.G. Xiong, Bandgap engineering of lead-halide perovskite-type ferroelectrics, Adv. Mater. 28 (2016) 2579–2586.

[23] K.Z. Du, Q. Tu, X. Zhang, Q. Han, J. Liu, S. Zauscher, D.B. Mitzi, Two-dimensional Lead(II) halide-based hybrid perovskites templated by acene alkylamines: crystal structures, optical properties, and piezoelectricity, Inorg. Chem. 56 (2017) 9291–9302.

[24] X.G. Chen, X.J. Song, Z.X. Zhang, P.F. Li, J.Z. Ge, Y.Y. Tang, J.X. Gao, W.Y. Zhang, D.W. Fu, Y.M. You, R.G. Xiong, Two-dimensional layered perovskite ferroelectric with giant piezoelectric voltage coefficient, J. Am. Chem. Soc. 142 (2020) 1077–1082.

[25] Z. Wang, H. Zhang, F. Wang, H. Cheng, W. He, Y. Liu, X. Huang, P. Li, Superior transverse piezoelectricity in a halide perovskite molecular ferroelectric thin film, J. Am. Chem. Soc. 142 (2020) 12857–12864.

[26] W.Q. Liao, Y.Y. Tang, P.F. Li, Y.M. You, R.G. Xiong, Large piezoelectric effect in a lead-free molecular ferroelectric thin film, J. Am. Chem. Soc. 139 (2017) 18071–18077.

[27] Q. Zhang, L. Chu, F. Zhou, W. Ji, G. Eda, Excitonic properties of chemically synthesized 2D organic-inorganic hybrid perovskite nanosheets, Adv. Mater. 30 (2018), 1704055.

[28] S. Yang, W. Niu, A.L. Wang, Z. Fan, B. Chen, C. Tan, Q. Lu, H. Zhang, Ultrathin two-dimensional organic-inorganic hybrid perovskite nanosheets with bright, tunable photoluminescence and high stability, Angew. Chem. Int. Ed. 56 (2017) 4252–4255.

[29] X. Fu, S. Jiao, Y. Jiang, L. Li, X. Wang, C. Zhu, C. Ma, H. Zhao, Z. Xu, Y. Liu, W. Huang, W. Zheng, P. Fan, F. Jiang, D. Zhang, X. Zhu, X. Wang, A. Pan, Large-scale growth of ultrathin low-dimensional perovskite nanosheets for high-detectivity photodetectors, ACS Appl. Mater. Interfaces 12 (2019) 2884–2891.

[30] S. Deswal, S.K. Singh, R. Pandey, P. Nasa, D. Kabra, B. Praveenkumar, S. Ogale, R. Boomishankar, Neutral 1D perovskite-type ABX3 ferroelectrics with high mechanical energy harvesting performance, Chem. Mater. 32 (2020) 8333–8341.

[31] R.G. Kepler, R.A. Anderson, Ferroelectric polymers, Adv. Phys. 41 (1992) 1–57.

[32] I.O. Pariy, A.A. Ivanova, V.V. Shvartsman, D.C. Lupascu, G.B. Sukhorukov, T. Ludwig, A. Bartasyte, S. Mathur, M.A. Surmeneva, R.A. Surmenev, Piezoelectric response in hybrid micropillar arrays of poly(vinylidene fluoride) and reduced graphene oxide, Polymers 11 (2019) 1065.

[33] H. Röhm, T. Leonhard, M.J. Hoffmann, A. Colsmann, Ferroelectric domains in methylammonium lead iodide perovskite thin-films, Energy Environ. Sci. 10 (2017) 950–955.

[34] Y. Zhou, W. Liu, X. Huang, A. Zhang, Y. Zhang, Z.L. Wang, Theoretical study on two-dimensional MoS2 piezoelectric nanogenerators, Nano Res. 9 (2016) 800–807.

[35] W. Wu, L. Wang, Y. Li, F. Zhang, L. Lin, S. Niu, D. Chenet, X. Zhang, Y. Hao, T. F. Heinz, J. Hone, Z.L. Wang, Piezoelectricity of single-atomic-layer MoS2 for energy conversion and piezotronics, Nature 514 (2014) 470–474.

[36] H. Zhu, Y. Wang, J. Xiao, M. Liu, S. Xiong, Z.J. Wong, Z. Ye, Y. Ye, X. Yin, X. Zhang, Observation of piezoelectricity in free-standing monolayer MoS2, Nat. Nanotechnol. 10 (2015) 151–155.

[37] R. Quintero-Bermudez, A. Gold-Parker, A.H. Proppe, R. Munir, Z. Yang, S. O. Kelley, A. Amassian, M.F. Toney, E.H. Sargent, Compositional and orientational control in metal halide perovskites of reduced dimensionality, Nat. Mater. 17 (2018) 900–907.

[38] M. Wu, T. Zheng, H. Zheng, J. Li, W. Wang, M. Zhu, F. Li, G. Yue, Y. Gu, J. Wu, High-performance piezoelectric-energy-harvester and self-powered mechanosensing using lead-free potassium–sodium niobate flexible piezoelectric composites, J. Mater. Chem. A 6 (2018) 16439–16449.

[39] H. Han, C. Voisin, S. Guillemet-Fritsch, P. Dufour, C. Tenailleau, C. Turner, J. C. Nino, Origin of colossal permittivity in BaTiO3 via broadband dielectric spectroscopy, J. Appl. Phys. 113 (2013), 024102.

[40] B. Dutta, E. Kar, N. Bose, S. Mukherjee, NiO@SiO2/PVDF: a flexible polymer nanocomposite for a high performance human body motion-based energy harvester and tactile e-skin mechanosensor, ACS Sustain. Chem. Eng. 6 (2018) 10505–10516.

[41] G. Zhang, Q. Liao, Z. Zhang, Q. Liang, Y. Zhao, X. Zheng, Y. Zhang, Novel piezoelectric paper-based flexible nanogenerators composed of BaTiO3 nanoparticles and bacterial cellulose, Adv. Sci. 3 (2016), 1500257.

[42] Z.H. Lin, Y. Yang, J.M. Wu, Y. Liu, F. Zhang, Z.L. Wang, BaTiO3 nanotubes-based flexible and transparent nanogenerators, J. Phys. Chem. Lett. 3 (2012) 3599–3604.

[43] W. Zhang, H. Yang, Li Li, S. Lin, P. Ji, C. Hu, D. Zhang, Y. Xi, Flexible piezoelectric nanogenerators based on a CdS nanowall for self-powered sensors, Nanotechnology 31 (2020), 385401.

[44] N. Wang, W. Dou, S. Hao, Y. Cheng, D. Zhou, X. Huang, C. Jiang, X. Cao, Tactile sensor from self-chargeable piezoelectric supercapacitor, Nano Energy 56 (2019) 868–874.

[45] Y. Han, C. Gao, H. Zhu, S. Chen, Q. Jiang, T. Li, M. Willander, X. Cao, N. Wang, Piezotronic effect enhanced nanowire sensing of H2O2 released by cells, Nano Energy 13 (2015) 405–413.

[46] Y. Xi, J. Song, S. Xu, R. Yang, Z. Gao, C. Hu, Z.L. Wang, Growth of ZnO nanotube arrays and nanotube based piezoelectric nanogenerators, J. Mater. Chem. 19 (2009) 9260.

[47] S. Hao, J. Jiao, Y. Chen, Z.L. Wang, X. Cao, Natural wood-based triboelectric nanogenerator as self-powered sensing for smart homes and floors, Nano Energy 75 (2020), 104957.

Asif Abdullah Khan is a Ph.D. candidate and NSERC Vanier scholar, under the supervision of Professor Dayan Ban in the Department of Electrical and Computer Engineering, University of Waterloo, Canada. In 2015, he received his Bachelor of Science degree in Electrical and Electronic Engineering (EEE) from Khulna University of Engineering & Technology (KUET), Khulna, Bangladesh. His research includes synthesis and characterization of advanced energy materials for high-performance nanogenerators and self-powered wireless sensing systems for IoT applications.

Dr. Guangguang Huang is currently an Associate Professor in the Key Laboratory for Special Functional Materials of the Ministry of Education at Henan University. From 2014–2019, he pursued M.S. and Ph.D. degree in the Advanced Photonic Center at Southeast University, supervised by Prof. Chunlei Wang and Prof. Yiping Cui. In 2019, he became a Postdoctoral Fellow at the University of Waterloo, Canada. His current research interests concentrate on piezoelectric photonic crystals and flexible devices.

Dr. Nicolas Tanguy completed his Ph.D. at the University of Toronto and is now a Post-Doctoral Fellow in the Research in Advanced Biomaterials and Biochemicals Laboratory. His topics of interest involve the design of green electronics devices, the synthesis of conductive polymer and carbon-based nanocomposites, the design of gas sensors and the transfer of novel materials and nanocomposites to wireless communication systems.

Md. Masud Rana received his M.Sc. and B.Sc. degree in Electrical and Electronic Engineering, from Khulna University of Engineering and Technology (KUET), Bangladesh. During his M.Sc. degree, his research was focused on vibrational properties of Graphene and related 2D materials, their modeling and characterization. Currently, he is doing his Ph.D. in Electrical and Computer Engineering – Nanotechnology at the University of Waterloo under the supervision of Prof. Dayan Ban. His current research focuses on the synthesis and characterization of piezoelectric, triboelectric energy harvester, and their utilization in various energy and environmental applications.

Dr. Bin Sun is now a postdoc fellow under Prof. Ted Sargent at the University of Toronto. He received his Ph.D. in Chemical Engineering at the University of Waterloo, Ontario, Canada. His Ph.D. research was focused on polymer semiconductor development and field-effect transistor engineering. He is currently working on solution-processed colloidal quantum dots-based photo-harvesting devices.

Nanqin Mei is a Ph.D. student in Physics-Nanotechnology, Department of Physics and Astronomy, University of Waterloo, Canada. She holds a joint Bachelor's degree in Science from the University of Waterloo and Beijing Jiaotong University, China and currently is doing her Ph.D. research in biophysics and nanotechnology using atomic force microscopy (AFM) and Kelvin probe microscopy (KPFM) and other biophysical techniques.

Dr. Zoya Leonenko is a Professor and University Research Chair in the Department of Physics and Astronomy, University of Waterloo, Canada. She did her undergraduate study at the Novosibirsk State University and Ph.D. at the Institute of Chemical Kinetics and Combustion, Novosibirsk, Russian Academy of Sciences. Currently, she leads an active research laboratory with expertise in atomic force microscopy, Kelvin probe force microscopy, biophysics and biomedical nanotechnology at the University of Waterloo, and is a President of the Biophysical Society of Canada.

Margherita Biondi is a Ph.D. student in the group of Prof. Ted Sargent in the Department of Electrical and Computer Engineering at the University of Toronto. She received her B.Sc. in Materials Science and M.Sc. in Materials Science and Engineering from Università Degli Studi di Genova, Italy. Her current research is focused on quantum dots for optoelectronic devices.

Dr. Ning Yan holds a University of Toronto Distinguished Professorship in Forest Biomaterials Engineering at the Department of Chemical Engineering and Applied Chemistry. She was also an Endowed Chair in Value Added Wood and Composites. Professor Yan has published more than 180 peer-reviewed journal papers. She is an international expert on forest biomaterial science and bio-based products. She is currently the Director of the Low Carbon Renewable Materials Centre in the Faculty of Applied Sciences and Engineering. Dr. Yan obtained her Ph.D. from the Department of Chemical Engineering and Applied Chemistry of the University of Toronto in 1997.

Dr. Shazzad Rassel completed his MSc and Ph.D. from the University of Oklahoma, Oklahoma, USA in 2013 and 2018, respectively. He received his BS degree from the Islamic University of Technology, Dhaka, Bangladesh in 2002. At present, he is working as a Mitacs Research fellow at the University of Waterloo, Canada. His research interests include interband and intersubband-based lasers and detectors in the mid-IR and THz region, biosensors, and photoacoustic spectroscopy.

Dr. Chunlei Wang received his B.A. at Jilin University in 2003. Then, he began the graduate study in state key laboratory of supramolecular and structure and materials at Jilin University. After received his Ph.D. in 2008, he became a formal faculty of Southeast University in China. After then, he got a promotion to an Associate Professor and Professor in 2012 and 2016, respectively. From 2017–2018, he became a visiting scholar at the Quantum Nano Centre at the University of Waterloo in Canada. His current research interest is the synthesis and application of luminescent nanocrystals.

Dr. Shuhong Xu received her Bachelor's degree in 2003 and Master's degree in 2006 at the College of Chemistry of Jilin University. After that, she received her Ph.D. degree in 2015 at Southeast University, and then she became a formal faculty of the School of Electronic Science and Engineering of Southeast University to now. She got a promotion to an Associate Professor in 2016. From 2017–2018, she became a visiting scholar at the Quantum Nano Centre at the University of Waterloo in Canada. Her current research interest is photoelectric functional materials and their applications.

Dr. Dayan Ban is a Professor in the Department of Electrical and Computer Engineering at the University of Waterloo. Dayan Ban earned BASc, MASc degrees at the University of Science and Technology of China, Hefei, China in 1993 and 1995, respectively and Ph.D. degree at the University of Toronto in 2003. He was a visiting scientist at the Research Laboratory of Electronics (RLE) at MIT, Cambridge, MA, USA in 2009. His current research interests include optoelectronics, semiconductor quantum devices, terahertz quantum cascade lasers, infrared optical up conversion devices, Infrared imaging devices, scanning probe microscopy, nanotechnology and nanofabrication.